PROCEEDINGS OF SPIE

SPIEDigitalLibrary.org/conference-proceedings-of-spie

Broadband coated lens solutions for FIR-mm-wave instruments

Alexey Shitvov, Giorgio Savini, Peter Hargrave, Peter Ade, Carole Tucker, et al.

Alexey Shitvov, Giorgio Savini, Peter C. Hargrave, Peter A. R. Ade, Carole E. Tucker, Rashmi V. Sudiwala, Jin Zhang, Jon E. Gudmundsson, Berend Winter, Giampaolo Pisano, Maarten van der Vorst, "Broadband coated lens solutions for FIR-mm-wave instruments," Proc. SPIE 12190, Millimeter, Submillimeter, and Far-Infrared Detectors and Instrumentation for Astronomy XI, 121900D (31 August 2022); doi: 10.1117/12.2629968

SPIE.

Event: SPIE Astronomical Telescopes + Instrumentation, 2022, Montréal, Québec, Canada

Broadband coated lens solutions for FIR-mm-wave instruments

Alexey Shitvov*[a], Giorgio Savini[a], Peter C. Hargrave[b], Peter A. R. Ade[b], Carole E. Tucker[b], Rashmi V. Sudiwala[b], Jin Zhang[c], Jon E. Gudmundsson[d], Berend Winter[e], Giampaolo Pisano[f], Maarten van der Vorst[g]

[a]Dept. of Physics and Astronomy, University College London, Gower Street, London WC1E 6BT, UK; [b]Dept. of Physics and Astronomy, Cardiff University, Queen's Buildings North, 5 The Parade, Newport Road, Cardiff, CF24 3AA, UK; [c]School of Computing and Information Science, Anglia Ruskin University, East Road, Cambridge, CB1 1PT, UK; [d]Stockholm University and the Oskar Klein Centre, AlbaNova University Centre, Roslagstullsbacken 21, 106 91, Stockholm, Sweden; [e]Dept. of Space and Climate Physics, Mullard Space Science Laboratory, University College London, Holmbury St. Mary, Dorking, Surrey RH5 6NT, UK; [f]Dipartimento di Fisica, Sapienza Universit`a di Roma, Piazzale Aldo Moro 5, I-00185 Roma, Italy; [g]European Space Research and Technology Ctr., European Space Agency, Keplerlaan 1, PO. Box 299, 2200 AG, Noordwijk ZH, The Netherlands.

ABSTRACT

This paper presents recent results of ongoing European Space Agency funded program of work aimed at developing large dielectric lenses suitable for future satellite missions, with a particular focus on requirements for CMB polarimetry. Two lens solutions are being investigated: (i) polymer lenses with broadband multi-layer antireflection coatings; (ii) silicon lenses with surface-structured anti-reflection coating represented by directly machined pyramidal features. For each solution, base materials with and without coatings have been optically characterized over a range of temperatures down to ~10 K. Full lens solutions are under manufacture and will be tested in a bespoke large cryo-optical facility.

Keywords: anti-reflection coating, cosmic microwave background, dielectric characterization, dielectric lens, millimeter-wave astronomy, quasi-optical systems, refracting telescope

1. INTRODUCTION

Large cryogenic quasi-optical elements, such as dielectric lenses, half-wave plates, and thermal filters, are the key components of emerging millimeter-astronomy instruments at the heart of a number of current and future missions. Their development constitutes not a straightforward scaling duplication of the existing solutions, but an involved constrained design aimed to achieve instrument performance surpassing the state-of-the-art specifications by orders of magnitude. Although the work presented in this paper applies to a range of instruments and missions, for the present purpose we focus on dielectric lenses for the Light satellite for the studies of B-mode polarization and Inflation from cosmic background Radiation Detection (LiteBIRD) mission [1] scheduled for launch at the end of the decade.

The quest for ever more precise observations of cosmic microwave background (CMB) anisotropies has long been a mainspring of millimeter-astronomy instrumentation. A family of ground-based, balloon-borne, and space missions have been successfully deployed and still produce a steadily growing body of scientific data, even long after decommissioning of the respective instruments, pushing the boundaries of our understanding of the origins of the home universe and how it works. First observations of the isotropic black-body CMB radiation, following the discovery of CMB in 1965, prompted the concept of a dense and hot early universe and set the scene for the modern cosmology. The following observations of the CMB temperature fluctuations, pioneered by the Cosmic Background Explorer (COBE) mission in 1992, led to the development of the standard cosmological model and provided critical insights in the origins of the structure, baryon density, dark matter and dark energy, neutrino flavors, and the global properties of spacetime. As the knowledge well of the CMB temperature fluctuations had been exhausted, while leaving some fundamental questions yet unresolved, the new

* a.shitvov@ucl.ac.uk; www.ucl.ac.uk/astrophysics/people/dr-alexey-shitvov

Millimeter, Submillimeter, and Far-Infrared Detectors and Instrumentation for Astronomy XI, edited by Jonas Zmuidzinas, Jian-Rong Gao, Proc. of SPIE Vol. 12190, 121900D · © 2022 SPIE · 0277-786X · doi: 10.1117/12.2629968

era of observations of much fainter CMB polarization anisotropies had come, prompted by the rapid progress of millimeter-astronomy instrumentation.

One of the key questions of the early universe is the origin of the primordial fluctuations that developed into the observed CMB anisotropies and later gave birth to the stars and galaxies. The leading cosmological inflation theory speculates a mechanism of exponential expansion of minute quantum fluctuations in microscopic spacetime regions of the very early universe into the universe filled with nearly homogeneous and isotropic cold plasma, with weak traces of the primordial quantum fluctuations imprinted into the fabric of the modern universe.

From the theoretical standpoint, the CMB radiation is linearly polarized at ~10% level due to Thomson scattering of photons off free electrons in the surface of last scattering. The CMB polarization, first detected by the Degree Angular Scale Interferometer (DASI) deployed at the South Pole in 2002, exhibits spatial anisotropies which can be cast invariantly into two components, according to their properties under parity transformation – so called 'E-modes' and 'B-modes'. The E-mode polarization is the strongest constituent predominantly caused by acoustic waves present at recombination, and its signal is strongest at the angular scales of a few to tens arcminutes (corresponding to multipole moments l~1000). The primordial B-mode polarization is about two orders of magnitude lower, and it is caused by the imprinted pattern of the gravitational waves, peaking on degree angular scales (corresponding to the 'recombination peak' near l~80) and on very large angular scales (corresponding to the 'reionization' peak at low l<10). Direct observations of the B-mode polarization are hampered by several factors, including weak gravitational lensing (converting E-mode polarization into B-mode) and foreground sources (thermal emission by interstellar dust medium at frequencies > 100 GHz and synchrotron emission at lower frequencies). However, distinctively different frequency dependences of B-mode and foreground polarization signals allow for their disentanglement by means of multi-spectral observations. The more recent series of ground-based Background Imaging of Cosmic Extragalactic Polarization (BICEP) experiments, along with the Planck satellite mission, provided critical data on the foreground modelling and removal. Essentially, ground-based experiments can only target the recombination peak, while the space missions can see both peaks in the B-mode angular spectrum. In this respect, the Planck satellite heritage constitutes a treasure trove of the millimeter-astronomy in space with many critical lessons learned on the instrument systematics and calibration.

Detection of the primordial gravitational waves through observations of the B-mode polarization anisotropy will have profound effect on modern science in many fields of fundamental physics. However, to make this happen, new full-sky CMB observations in space must be 30 times more sensitive than previous full-sky missions. Given that the new generation of instruments are not limited by detector sensitivity, but rather by interplay of the foreground and instrument systematics effects, detailed knowledge of the instrument performance, from the materials and components through the sub-systems and to the system level impairments, is imperative for future successful missions.

LiteBIRD comprises a suite of three instruments to survey the full sky in 15 frequency channels spanning 34 to 448 GHz with effective polarization sensitivity of 2 μK-arcmin and angular resolution of 31 arcmin (at 140 GHz). A key feature of the design of each instrument is the use of rapid polarization modulation by means of continuously rotating half-wave plate (CRHWP). In combination with the stable operating environment at the orbit around the second Lagrangian point for the Sun-Earth system, polarization modulation will provide unprecedented level of control of the systematic errors, particularly on the largest angular scales, although CRHWP non-idealities may introduce new systematics, which require accurate modelling and calibration.

The LiteBIRD's low-frequency telescope (LFT), operating in the 34-161 GHz frequency band attaining an angular resolution of 24-71 arcmin, features a high-end reflective type architecture based on the Crossed Dragone Telescope optical design, which preserves polarization by means of compensation and provides a large field of view (FoV) in a compact volume. On the contrary, medium-frequency (MFT) and high-frequency (HFT) telescopes, operating in the frequency bands of 89-224 GHz and 166-448 GHz, respectively, are, essentially, two-lens refractor telescopes capable of achieving better than 30 arcmin angular resolution across the respective frequency bands. The use of refractive optics for the LFT architecture is not feasible within the payload specification, particularly, due to the volume and mass constraints.

The choice of the fully refractive MHFT configuration was driven by the extensive expertise of current and perspective sub-orbital CMB instruments, as well as by technical advantages of the on-axis refracting configuration, notably, superior resolving power per inch of the aperture, high optical throughput, higher focal plane area utilization, and inherently low instrument polarization and differential beam parameters, [2], owing to the axial symmetry of the telescope. The two-lens refractor configuration allows a compact ~f/2.2 telecentric optical design meeting the volume and weight constraints of the LiteBIRD payload budget, as well as efficient mitigation of straylight issues. The use of the two telescope tubes with

overlapping frequency bands is mainly dictated by the broadband performance of the CRHWP and anti-reflection coatings of the lenses, achievable under specific technological constraints. It is noteworthy that the perspective lens materials do not exhibit discernible frequency dispersion in the millimeter-frequency range, thus no significant chromatic aberrations, otherwise pertaining to the refractive optics, were anticipated. Still, monochromatic optical aberrations, particularly field curvature, persist. Another advantage of having two telescopes stems from the ease of the optimum design of thermal filter stacks, as well as assembly, integration, testing, and verification of the asset.

The LiteBIRD specified 28°field of view, <30 arcmin angular resolution, minimum straylight and reflection artefacts, as well as mass and volume constraints prescribed by the cooling power and payload specification, have been implemented in the optimum optical designs of the MFT and HFT two-lens refractor telescopes, [3]. It was noted, e.g., [4], that although using three lenses can potentially lead to even lower optical aberrations, the additional lens surfaces may cause undesirable optical artefacts, such as 'optical ghosting', due to non-ideal anti-reflection coating (ARC) of the lenses, [3]. A tilted-element optics architecture, [5], can help reduce optical ghosting, although at the expense of higher optical aberrations. Besides, the asset loses its axial symmetry which may increase instrument systematics. The use of free-form lenses, e.g., [6] and [7], particularly, to compensate optical aberrations pertaining to the tilted elements, requires a holistic design approach and significantly complicates instrument implementation and characterization. This draws special attention to developing frequency, angle, and polarization insensitive means of minimizing optical reflections from the lens surfaces and respective manufacturing technologies. This paper presents research in progress aimed to address the growing demand for versatile broadband anti-reflection coating solutions for large cryogenic optics of the emerging CMB astronomy instruments.

2. LENS MATERIALS AND CHARACTERIZATION

2.1 Test materials

The current baseline design of the LiteBIRD MFT and HFT instruments envisions the use of polymer lenses, made of either high-density polyethylene (HDPE) or ultra-high molecular weight polyethylene (UHMWPE) materials, [1] and [3]. Polypropylene (PP) was also considered as an alternative material, due to its higher melting temperature, [8]. The latter feature is advantageous for the ARC fabrication, which involves a multi-layer heat-bonding process, [9]. However, slightly higher thermal conductivity and lower coefficient of thermal expansion (CTE) of HDPE and UHMWPE at cryogenic temperatures, [10] and [11], make the latter materials preferable for the cold optics of CMB telescopes. Both PP and PE are low-index materials and feature low loss and low dispersion at millimeter-wave frequencies. Concerns regarding possible optical birefringence of polymers, both imprinted in the polymerization process and stress-induced upon cooling, [12], and the respective instrument systematics were previously addressed by measurements reported in [9].

Alternative to low-index polymers at millimeter frequencies are high-index crystalline materials, such as silicon and alumina, both extensively used in various CMB instruments, [13] and [14]. These materials feature extremely low loss and birefringence at millimeter frequencies, as well as significantly higher thermal conductivity and lower CTE as compared with pure polymers (semi-crystalline and amorphous). However, due to the higher refractive index, crystalline materials exhibit much higher reflection loss, as well as higher cross-polarization at oblique incidence, [15], causing undesirable polarization aberrations in axially symmetric optical systems, which can be deduced from the analysis of the Fresnel equations, [16].

In this work, complex refractive indexes of three lens materials, UHMWPE and PP polymers and high-resistivity silicon, have been measured as functions of temperature and frequency, using the experimental setups and methodologies presented in the next section. The UHMWPE material was supplied by Ensinger Machined Parts Ltd under the trademark 'TECAFINE PE 1000 natural' certified for general construction and food industries. The material was pre-annealed before delivery by the vendor in a large block in a convection oven for 16 hours at ~105°C. The pre-annealing treatment was aimed at preventing noticeable change of the refractive index of the lens body due to the ARC heat-bonding process. The effect of thermal history on the internal structure and mechanical properties of semi-crystalline polymers has been extensively studied in the past and it has been shown that properly designed thermal annealing may cause increased content of crystalline phase, the state of relaxation of the non-crystalline phase, the linkage of the crystalline areas and the spherulites, and the state of internal stress on spherulite boundaries, thus increasing the secant modulus of elasticity, [17]. The annealed polymer stock provides reference values of the complex refractive index and will be used for manufacturing all lenses which will be installed on the working instrument, thus minimizing the respective index uncertainties and sub-optimum lens performance.

The reference PP material was also supplied by Ensinger Machined Parts Ltd under the trademark 'TECAFINE PP natural' certified for food, chemical and pharmaceutical industries. The material is heat-stabilized semi-crystalline homopolymer and it was pre-annealed in the same way as the above UHMWPE stock and delivered in a single block.

Plane-parallel sample slugs for material characterization and test biconvex lenses made of the reference polymers were lathed out of the vendor's blanks by the in-house workshop. All polymer slugs had 75 mm diameter to fit the clear aperture of the custom-design variable temperature testbed (VTT). The aperture diameter was chosen to fit the test beam of the Fourier transform spectrometer (FTS) testbed. The test slugs were subjected to measurement of planarity, parallelism, and surface roughness, which may introduce uncertainty in the retrieved dielectric parameters.

The reference silicon material for this study was sourced from a single boule of undoped high-resistivity float-zone silicon (HRFZ) supplied by Topsil Global Wafer A/S under trademark 'HiRes™'. According to the manufacturer's specification, this material features low oxygen levels and bulk room-temperature resistivity approaching 70 kΩ·cm, and it is certified for a range of active devices and passive components at millimeter and terahertz frequencies. The procured boule was suitable for cutting into slugs and wafers of up to 200 mm diameter. The choice of the float-zone silicon for cryogenic lenses over Czochralski (Cz) silicon was driven by the reasoning that the higher purity of HRFZ silicon should correlate with higher resistivity and lower loss, due to lower carrier scattering, [18], although it has been shown, *ibid*., that at low cryogenic temperatures ~4 K the bulk conductivity of silicon would freeze out and the dielectric loss will be similarly low, regardless of resistivity. On the other hand, high-resistivity Cz-silicon in experiments demonstrated superior radiation hardness against HRFZ and other grades of silicon, [19], which could be particularly relevant for space applications. All silicon samples had chemical-mechanical polishing applied to the faces of the slug, which was required for the ARC manufacture. The test procedures and parameter retrieval are described in the following section.

2.2 Dielectric measurement setups

Two quasi-optical testbeds have been employed for dielectric characterization. In both cases, the sample under test was placed inside the small cryogenic cavity of the variable temperature testbed, Fig. 1. The VTT was operated by a Sumitomo GM 4K cryocooler. To reduce the infrared thermal loading on the sample, the testbed was equipped with fixed blackened snouts to the input and output sides of the filter second stage mounts. Additionally, tilted thermal filters were added to all three thermal stages. A blackened environment thermometer was added, suspended by low thermal conductivity wires in the free space in the cavity and acting essentially as a bolometer to measure the effective thermal radiation environment. The VTT cooldown test results are shown in Fig. 2(a).

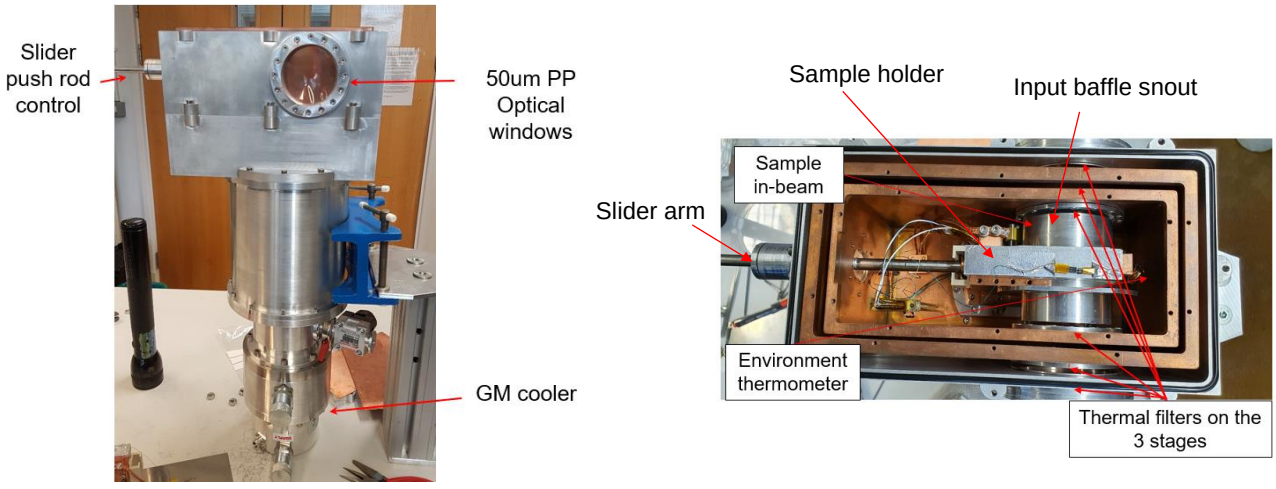

(a) (b)

Figure 1. The view of the variable temperature testbed: (a) inverted VTT with the Sumitomo GM 4K cooler beneath; (b) the VTT interior with the sliding sample holder shown with the sample in the beam.

The sample slider is thermally isolated from the base using a G10 bearing and is cooled via a flexible copper braid. The slider is fitted with a heater and a thermometer to enable PID control to set temperatures. This allows steady sample temperatures to be maintained during the recording of spectral data. Sample temperatures up to 100 K were withing direct range of the system. To access higher temperatures, the heating loop was modified to prevent a detrimental effect on the cooler. At higher temperatures, the increased heat capacity of the sample requires significantly longer settling time. An example thermal run under PID control is shown in Fig. 2(b).

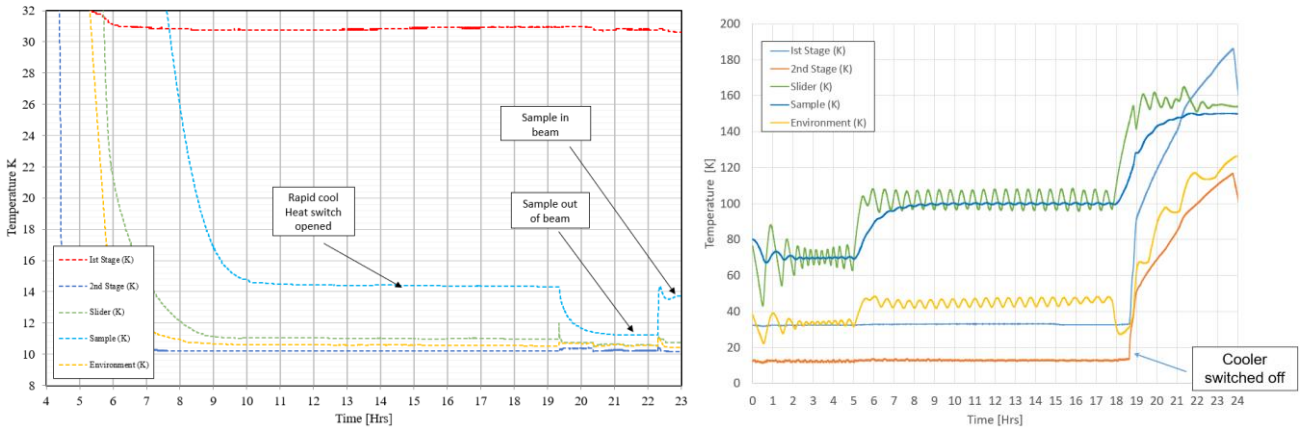

(a) (b)

Figure 2. Results of thermal characterization of the variable temperature testbed: (a) the cooldown results for the working system; (b) example thermal data for a typical run under PID control.

One of the two quasi-optical testbeds was operated with a vector network analyzer (VNA) equipped with a set of millimeter-wave frequency extenders fitted with standard gain horn antennas which seamlessly covered a wide frequency range of 75-330 GHz. This permitted vector measurements of the transmission magnitude and phase. Measurements could be conducted in two configurations: (i) reflecting, using a pair of matched parabolic mirrors, Fig. 3(a); or (ii) transmitting, with a pair of matching HDPE lenses, Fig. 3(b). Both configurations produced a beam waist in the middle of the sample. Reduction of standing waves due to reflections from the thermal filters was achieved by tilting the VTT filters with respect to the input beam, alongside optimization of the filter stack configuration.

The second quasi-optical testbed employed a polarizing Fourier transform spectrometer (Martin-Puplett interferometer configuration) to conduct transmission and absorption spectroscopy, whereby interferograms are collected based on the measurements of the coherence of a radiative source using time-domain or space-domain measurements and Fourier-transformed into the frequency or wavelength spectra. The detailed description of the FTS testbed, calibration and dielectric parameter retrieval procedure can be found elsewhere, [9] and [11]. Here, it is only instructive to briefly revisit some important points and new features which had direct impact on the measured data.

In the transmission spectroscopy, measurements are performed with and without a sample in the beam, and their ratio allows removing all spectral features associated with the source emission and detector system. The VTT with the sample is located outside the main FTS chamber being isolated via a 50 μm mylar window, Fig. 4. A pair of matching HDPE lenses was used to implement a Gaussian beam telescope (GBT) optical configuration, allowing it to place the beam waist at the position of the sample under test, thus eliminating the need for correcting for the converging beam at the FTS output. The HDPE lens *f*-number was identical to that of the FTS beam, thus maximizing the optical throughput. In the paraxial GBT configuration, the beam propagates a given length through air at certain humidity and temperature levels, which may introduce measurement uncertainty and therefore need to be monitored during the test.

All measurements were performed in a spectral range of 3-40 cm^{-1} (corresponding to 90-1200 GHz), but with focus on the 3-20 cm^{-1} (90-600 GHz) region. The source is a Mercury-arc lamp with 0.9 mm quartz casing (~1800 K thermal black body) of 10 mm aperture, and an output beam of ~*f*/3.5. The *f*-number could be increased using a diaphragm aperture after the collimating mirror internal to the spectrometer, but this will result in reduction of throughput and signal-to-noise ratio.

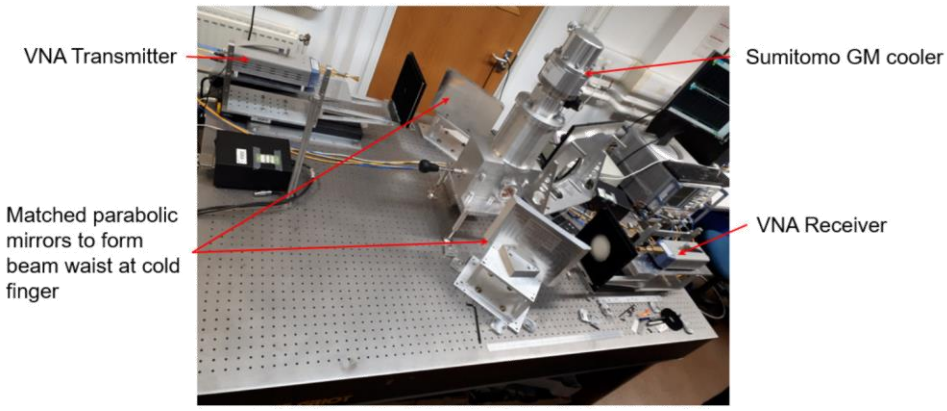

(a)

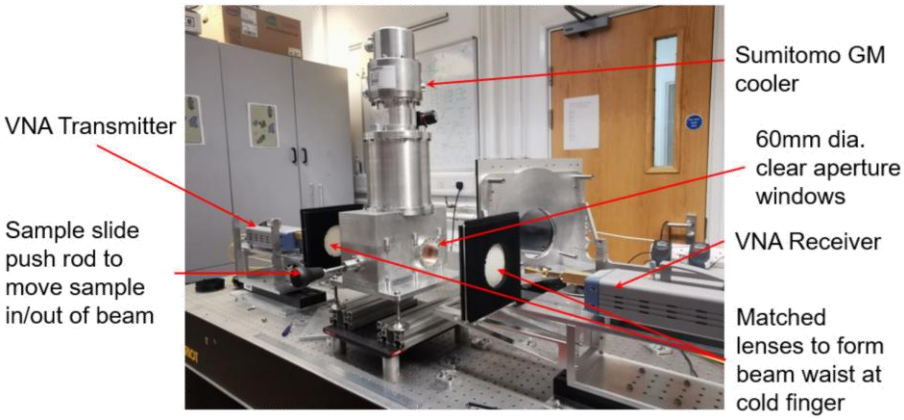

(b)

Figure 3. Quasi-optical VNA testbed configuration (a) with the pair of matching parabolic mirrors and (b) using a pair of matching HDPE lenses to form a beam waist at the cold sample position.

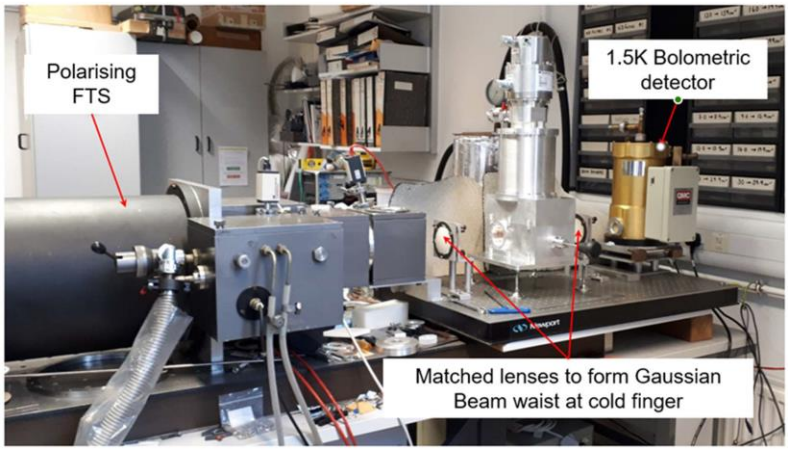

Figure 4. The FTS measurement configuration featuring two matched lenses forming a beam waist at the position of the sample under test placed inside the variable temperature testbed.

The conventional FTS operation implies acquisition of multiple interferograms which, after averaging, are Fourier-transformed to recover the spectrum. To remove all irrelevant spectral features attributed to the source and to the detecting system (a 4He-pumped 1.6 K Ge-NTD bolometer), a first 'background' set of data was taken without the sample in the beam, viz., with the open aperture inside the VTT. The background dataset inherits all spectral features of the source, VTT, and detecting system: black-body radiation with superimposed fringe features from the quartz casing of the lamp, the windows and wedged filter stacks of the VTT, the window and spectral filters installed in the detector cryostat, and the optical coupling of the detector to radiation via a Winston parabolic concentrator.

In a second measurement, the dielectric sample under test is pulled into the beam and a second spectrum is taken. This spectrum will contain all of the above features, plus additional Fabry-Pérot (FP) fringes caused by the standing waves due to the presence of the dielectric slab. The ratio of the two spectra is then taken to remove all undesired testbed contributions and leave the expected FP fringes typical of a flat slab interference pattern.

The FTS spectral resolution depends on the optical path difference (OPD) between the spectrometer arms. The empirical value of 20 cm OPD was chosen to achieve a trade-off between precision and measurement duration. The data are acquired by the detector as timelines in a 'fast scanning' mode which produces an asymmetric interferogram with scan duration of a few tens of seconds. The acquired interferograms are phase corrected. The power which is contained in the sine component is restored to the cosine part via convolution with a kernel obtained by adopting a linear fit to the phase obtained from Fourier transforming the central part of the interferogram. At this point the interferogram is apodized (viz., multiplied by a triangular scaling function) to ensure that its values at maximum OPD tend to zero, avoiding any Gibbs artefacts in the resulting spectrum.

Other effects on the output spectrum that need to be taken into account (to first order) include: (i) finite aperture size of the source, which reduce visibility of the fringes due to averaging of sets of fringes propagating with different angles; (ii) when applicable, converging beam on the sample, which manifests itself as an effective combination of many spectra associated with different populations of rays binned in different angles of incidence, resulting in a similar effect to (i) with additional second-order effect of a spatial walk-off. It is noteworthy that the analysis of reflection and transmission of a Gaussian beam in a dielectric slab is much more involved, as compared to the case of uniform plane waves. Probably the simplest analysis is that based on the angular-spectrum decomposition within the framework of the linear shift-invariant systems, whereby the incident beam is represented by a spatial spectrum of uniform plane waves each of which is reflected and propagated independently and contributes to the reconstructed spectrum of the reflected or transmitted beams, [20]. The transmitted beam exhibits various phase, amplitude and propagations effects, including lateral, focal, and angular shifts, the latter noticeable only for extremely narrow beams, as well as polarization effects. For this reason, tilted optics and higher curvature of the lens surfaces may require special consideration.

The dielectric parameter retrieval is carried out by FP fringe fitting using the following model of the dielectric slab transfer function that accounts for dielectric loss, [21]:

$$T = \left[\frac{\left(1-Re^{-\alpha d}\right)^2}{(1-R)^2 e^{-\alpha d}} + \frac{4R}{(1-R)^2}\sin^2(2\pi n\sigma d)\right]^{-1}, \quad (1)$$

which essentially represents a generalized Airy distribution for a FP resonator, [22]. In (1),

$$R = \left(\frac{1-n}{1+n}\right)^2$$

is the reflectivity of the dielectric slab d, - the slab thickness, n - the real-valued refractive index which depends on frequency, ν, $\sigma = 1/\lambda$ - a free-space wavenumber, and α - the power absorption per-unit-length coefficient, as per the Beer-Lambert law. In respect to the validity of model (1), one should note that it is derived on the assumption of uniform plane waves at normal incidence, which is applicable to the analysis of Gaussian beams with some caution. Moreover, in the analysis of a Gaussian beam impinging on an interface of dissimilar media, the beam is commonly assumed to be a fundamental TEM_{00} Gaussian mode. However, in reality, a paraxial Gaussian beam with uniform polarization in the transverse plane must have a small longitudinal component to satisfy the Maxwell equations, [23], although in practice, transverse beam approximation provides sufficient accuracy of analysis for sufficiently large beam waists.

In the previous measurement campaign, [9], the dielectric sample under test was placed at the focus of the FTS output and a correction for the converging beam was applied in postprocessing when needed. The respective refractive index was retrieved under assumption of being frequency independent, also it was observed, both in FP fringe fitting and by

comparing the index values averaged over different spectral ranges, that the refractive index of polymers exhibits slight increase with frequency.

In this paper, model (1) is fitted to the measured data and the first-order effects are accounted for by convolving the model results with an appropriate instrument-line function. An example of FP fringe fitting using model (1) is shown in Fig. 5. The dielectric measurement results are presented in the next section.

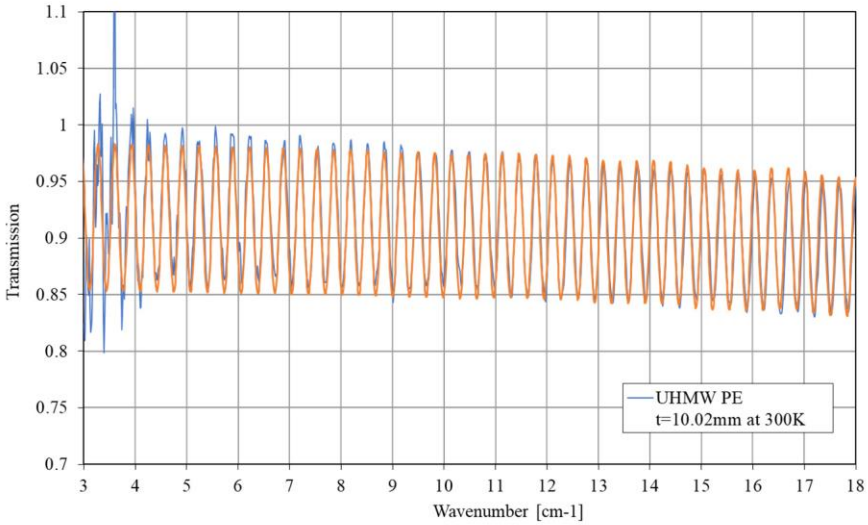

Figure 5. An example of frequency spectrum retrieved form FTS measurements for a 10.02 mm UHMWPE slab at room temperature. Blue curve is the measurement, red is model (1) convolved with the FTS instrument line function.

2.3 Dielectric measurement results

The measured temperature dependence of the UHMWPE refractive index for the 10.02 mm UHMWPE slab is shown in Fig. 6. The temperature dependence of the absorption coefficient, α, at three equally spaced frequencies is shown in Fig. 7. The measured absorption demonstrates non-monotonic behavior, which may indicate polymer crystallization at the lowest temperatures, but this cannot be confirmed by the optical measurement data alone and requires further analysis. The sag of the curves and minimum loss are increasing with frequency.

It is noteworthy that attempts to fringe-fit the dielectric loss coefficient were hampered by potential differences in optical coupling in the VTT, combined with the additional standing waves present in the setup. The inclusion of losses in FP model (1) would normally provide all necessary analytical tools to obtain the loss parameters, but the dependence on the data makes the fringe visibility and overall average transmission critical for this parameter to be well estimated. The issue is complicated by the fringe visibility being affected by the instrument line function and beam walk-off. That could be compensated to a degree by considering only the central part of the FTS interferogram, but this relies heavily on the stability of the source and detector.

It has been noted elsewhere that, in theory, non-polar polymers, to which UHMWPE arguably belongs based on its molecular structure, should exhibit a loss tangent that is both very low and frequency and temperature independent. However, nonmonotonic behavior has been observed in experiments. For instance, in [24] a small relaxation peak of the dielectric loss-tangent as a function of temperature was observed for a polyethylene sample in a temperature range from 90 to 200 K at 40 kHz. Its cause was attributed to the presence of carbonyl groups forming through accidental oxidation during the preparation of the polymer. Below 90 K, the loss-tangent was measured to be independent of frequency, hence indicating that no dipolar polarization existed, and that the specimen behaved as a pure non-dipolar material. Similar behavior of oxidized low-density polyethylene was reported in [25]. However, measurements conducted in [24] on a polyolefin sample (trademark ‘TPX’), which nominally features non-polar molecular structure and, seemingly, is polymerized in a process similar to polyethylene, alongside the weak relaxation peak in the same temperature region also

showed a distinctive minimum at ~65 K with a steady increase of the loss-tangent towards lower temperatures. This increase was tentatively attributed to a fast non-dipolar polarization, such as interfacial polarization of Maxwell-Wagner type, which could have been caused by contamination with metallic-compound catalysts used in the Zeigler polymerization process. Given that the UHMWPE material measured in this study was sourced from the general-industry stock, presence of some unwashed chemical additives would not be totally surprising. Further research is required to identify the nature of the millimeter-wave polarizability and loss at low temperatures.

The measurements are consistent with published data. In [26], a room-temperature refractive index $n = 1.537 \pm 0.009$ and an absorption coefficient $\alpha = 0.03 \pm 0.01$ cm^{-1} at 300 GHz (10 cm^{-1}) of UHMWPE were reported, measured with an FTS on samples of ca. 10, 20, and 30 mm thickness. A THz-range room-temperature refractive index $n = 1.5245$ and an absorption coefficient $\alpha = 0.135$ cm^{-1} of UHMWPE were reported in [27]. In [28], the respective room-temperature UHMWPE parameters measured at 1.5 THz were $n = 1.523$ and $\alpha = 0.148$ cm^{-1}. In [29], a room temperature refractive index $n \approx 1.521$ and an absorption coefficient $\alpha \approx 0.025$ cm^{-1} at 600 GHz ($\sigma = 20$ cm^{-1}) of a virgin 9.5 mm thick UHMWPE sample were measured using the terahertz time-domain spectroscopy (NB: these values are derived from the Cole-Cole plots in [29]). A drastic degradation of UHMWPE properties of samples subjected to γ-irradiation was observed. Notably, the increase of the absorption was interpreted to originate in the oxidation of the amorphous region within the sample.

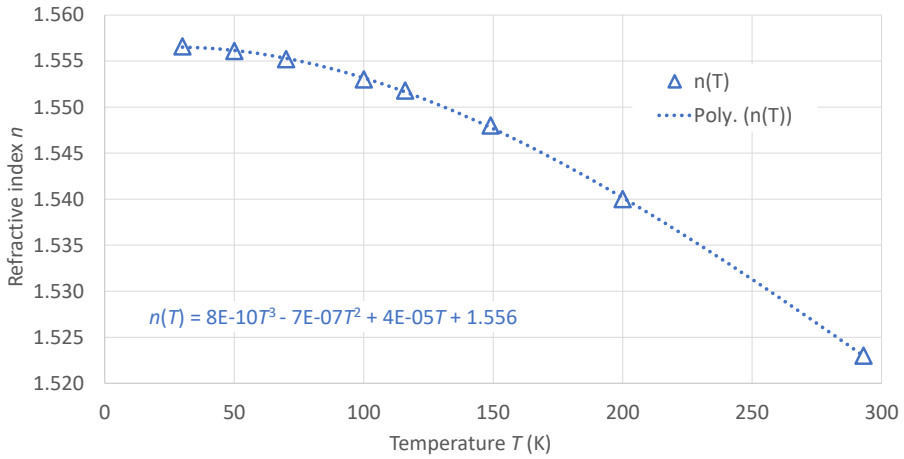

Figure 6. Temperature dependence of the spectral-averaged refractive index of UHMWPE retrieved from the FTS measurements of in 3-20 cm^{-1} range (10.02 mm thick dielectric slab, annealed).

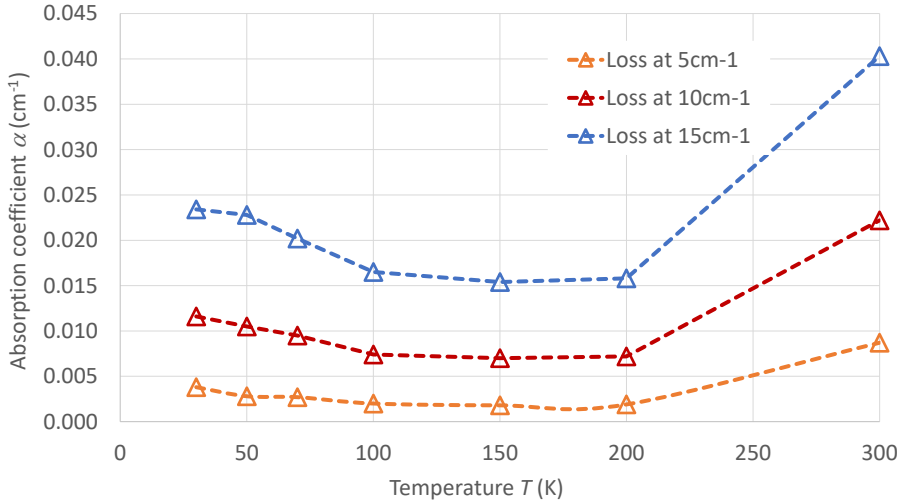

Figure 7. Temperature dependence of the absorption coefficient, α, of UHMWPE (10.02 mm dielectric thick, annealed) retrieved from the FTS measurements for selected frequencies, viz. 5, 10, and 15 cm^{-1}, corresponding to 150, 300, and 450 GHz, respectively.

The refractive index and absorption coefficient of polypropylene measured with a 9.976 mm slab of the solid PP material (annealed) are shown in Fig. 8 and 9. The data in Fig. 9 show similar trend to the UHMWPE material, c.f., Fig. 7, although the PP loss appears to be approximately two times higher. This naturally suggests UHMWPE as a better choice for the CMB telescope optics. The new data correspond well with published results. The room-temperature dielectric parameters of PP were measured in [30] using both VNA-based and THz time-domain spectroscopy testbeds in 0.1 – 1.6 THz range, showing the refractive index n = 1.513 - 1.515 and absorption coefficient α = 0.116 – 1.211 cm^{-1} across the frequency range. In [31], THz time-domain spectroscopy measurements of PP dielectric parameters yielded the room-temperature values at 1THz of the refractive index n = 1.50 and absorption coefficient α = 0.58 cm^{-1}. It was also found that a modified Debye model (Havriliak-Negami relaxation model) can describe both absorption and refraction spectra of amorphous polymers in the frequency range from 0.1 up to 3 THz.

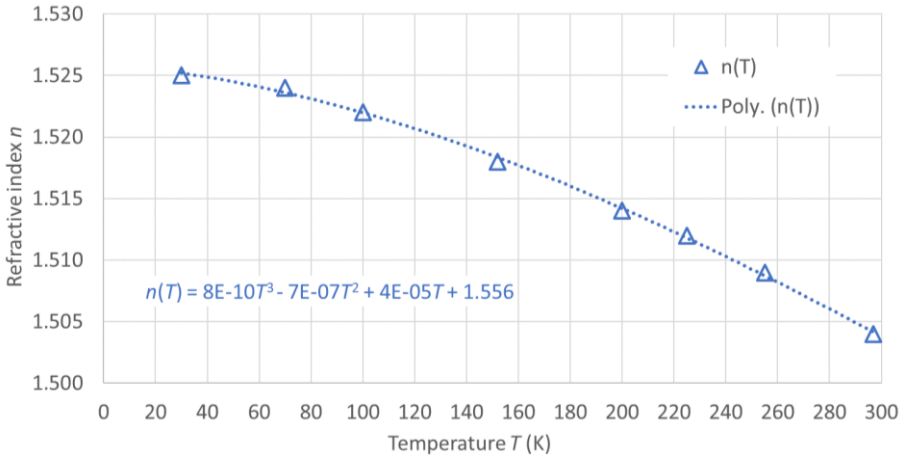

Figure 8. Temperature dependence of the spectral-averaged refractive index of PP (9.976 mm thick dielectric slab, annealed) retrieved from the FTS measurements in 3-20 cm^{-1} range.

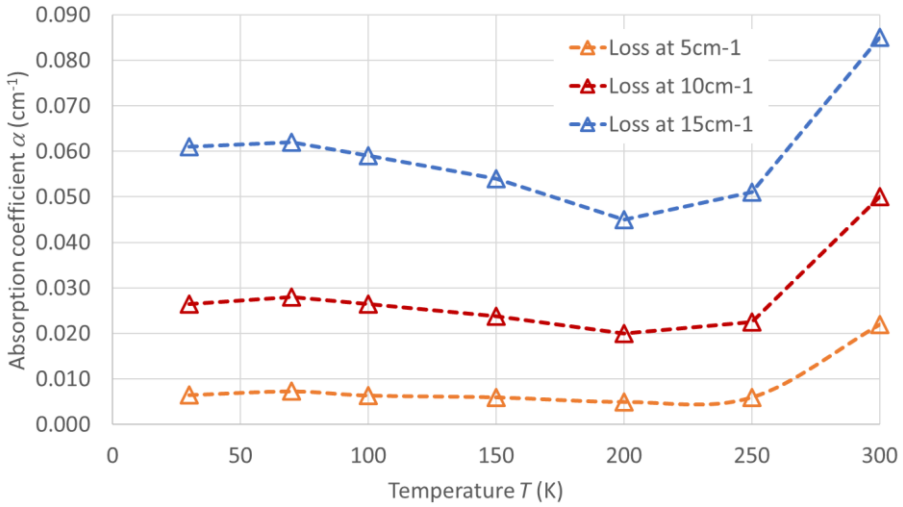

Figure 9. Temperature dependence of the absorption coefficient, α, of polypropylene (9.976 mm thick dielectric slab, annealed) retrieved from the FTS measurements for selected frequencies, viz. 5, 10, and 15 cm^{-1}, corresponding to 150, 300, and 450 GHz, respectively.

Measurements of the refractive index and loss-tangent of HRFZ-silicon were carried out on the 725 μm thick wafer (sample CB2.1 in Table 1). The respective spectral-averaged results are shown in Fig. 10 and 11. The loss-tangent was difficult to measure due to its extremely low value even at room temperature. Alternative measurements were carried out on a 11.92 mm thick HRFZ-silicon sample on the quasi-optical VNA testbed. The FP fringe fitting using model (1) convolved with the instrument line function is shown in Fig. 12 for the sample at room temperature. The best fit was achieved for a loss-tangent of 2×10^{-6}, which seems to be lower than indicated by the results in Fig. 11.

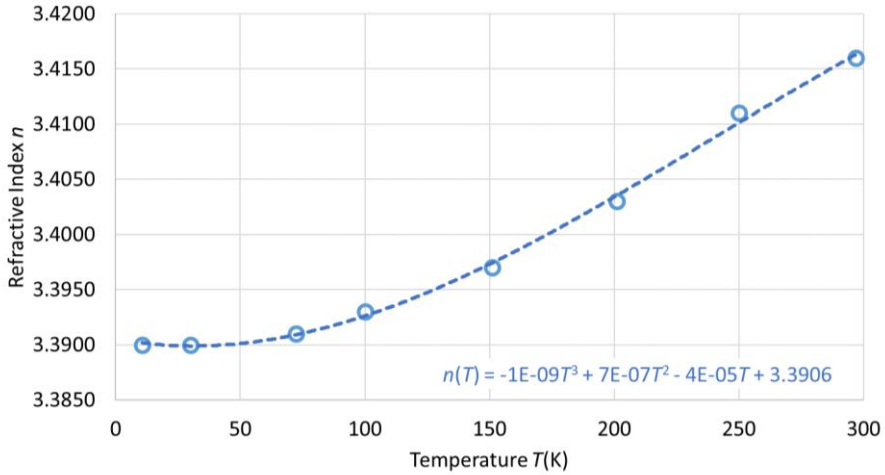

Figure 10. Temperature dependence of the spectral-averaged refractive index of HRFZ-silicon (750 μm thick dielectric slab) retrieved from the FTS measurements in 3-20 cm^{-1} range.

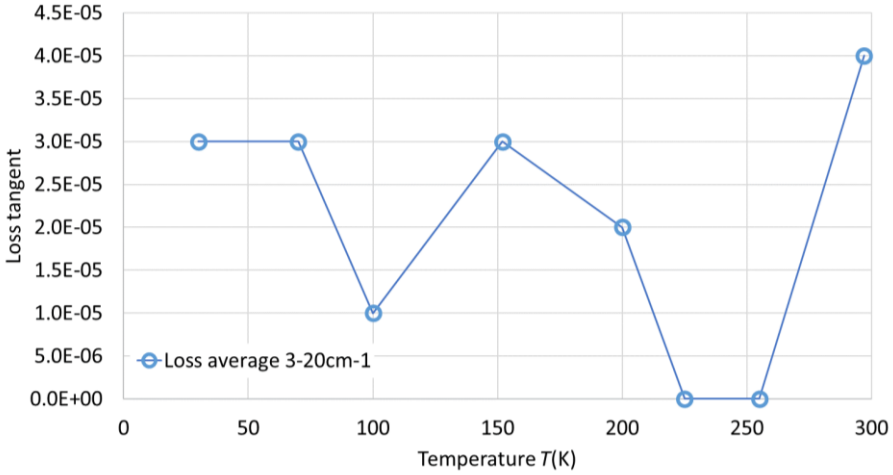

Figure 11. Temperature dependence of dielectric loss tangent of the HRFZ-silicon (750 μm thick dielectric wafer) retrieved from the FTS measurements.

The new data are in a reasonably good agreement with past studies, although the new loss-tangent values appear to be consistently lower in most cases. The FP resonator measurements in [32], conducted on p-type high-purity (HP) and n-type high-resistivity (HR) samples of FZ-silicon at room temperature, show monotonous decrease of the loss-tangent, as the frequency increases from 60 to 320 GHz, - from 5×10^{-5} to 1×10^{-5} for HPFZ-silicon and from 1.8×10^{-4} to 4×10^{-5} for HRFZ-silicon (c.f., spectral-averaged 4×10^{-5} in this work). The reported temperature dependence, *ibid.*, at 145 GHz

exhibits a non-monotonic behavior with a broad peak of ~8×10^{-5} at ~120 K and a minimum of ~6×10^{-5} at ~310 K for the HPFZ-silicon, and a peak of ~1.5×10^{-4} at ~150 K and a minimum of ~6×10^{-5} at ~290 K for the HRFZ-silicon (c.f., to the swing with temperature in Fig. 11). The respective room-temperature refractive index of the HRFZ-silicon specimen was measured near-linearly decreasing from 3.426 at 30 GHz to 3.415 at 300 GHz (c.f., spectral-averaged 3.416 in this work). The quasi-optical VNA measurements of high-resistivity (>70kΩ·cm) silicon in [33], carried out at room temperature in the frequency range 60-90 GHz, yielded the values of refractive index 3.423-3.429 (c.f., 3.416 in this work) and an average loss-tangent of ~2.1×10^{-3} (c.f., 4×10^{-5} in this work). The broadband quasi-optical VNA measurements in the refractive GBT configuration reported in [34] yielded the following refractive index/loss-tangent values for a 10.055 mm thick slab of high-resistivity silicon in 160-180 GHz frequency range at three sample temperatures: $3.422/2.3\times10^{-4}$ at 300 K (c.f., $3.416/4\times10^{-5}$ in this work); $3.398/6.8\times10^{-4}$ at 77 K (c.f., $3.391/3\times10^{-5}$ in this work); and $3.390/1.6\times10^{-4}$ at 4 K (c.f., $3.390/3\times10^{-5}$ at 30 K in this work).

The work is ongoing on experimental characterization of the dielectric materials using conventional empirical models compatible with simulation software, notably COMSOL Multiphysics. The FTS dielectric measurements can, in principle, provide a complete dataset for retrieval of temperature-dependent Sellmeier and thermo-optic coefficients of a broadband refractive index model, [35], to furnish accurate finite-element analyses with COMSOL of various quasi-optical components and systems of millimeter-astronomy instruments. More datasets are being derived from our recent measurements and will be reported elsewhere. Also, utility of a more comprehensive characterization of optical homogeneity, thermal, and mechanical properties of the lens polymers on large samples, instead of reliance on manufacturer or general published data, is being considered. The new data on lens dielectric parameters, along with the previous measurements in [9], is utilized in the next section in design of anti-reflection coatings.

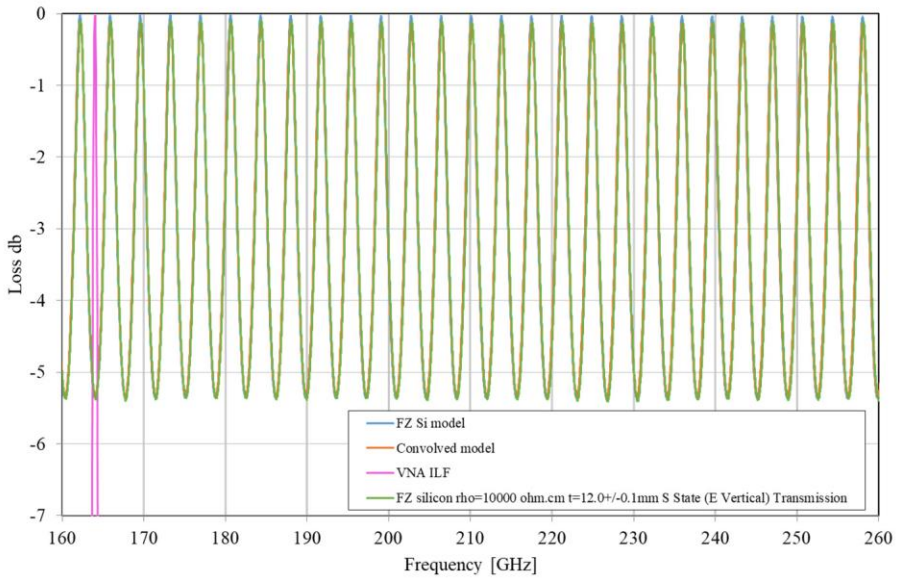

Figure 12. Spectral VNA measurement of 11.92 mm thick HRFZ-silicon sample. Measured data are plotted in green, and the model fit is plotted in amber; also shown are the VNA instrument line function (magenta) and transmission-line model of the slab (blue).

3. MULTI-LAYERED ANTIREFLECTION COATINGS

A mismatch of the wave impedances at the interface of free space and dielectric medium is the source of wave reflection which may cause detrimental issues with the system performance if not dealt with properly. Although reflected light can, in principle, be redirected and terminated off the main optical path, reduction of reflection from working optical surfaces, ensuring high optical throughput, still constitutes the mainstream design paradigm. This can be achieved by means of destructive interference of reflected waves or by gradient effective refractive index at the interface. Both means can be implemented with either stacked uniform dielectric layers or by surface structuring, or in a hybrid approach.

A multi-layer ARC comprises a stack of thin dielectric layers attached to the surface of the optical element, [36]-[38]. In general, refractive index and thickness of each layer can vary arbitrarily and both are subject of careful selection through a holistic design approach. The latter permits rigorous analytical treatment, e.g., using high-order transfer functions, [36], for a small number of dielectric layers and requires extensive numerical optimization for a larger number of dielectric layers. Theoretically, multi-layer ARC design shares a degree of commonality with design of microstrip impedance transformers. Arbitrary low reflection, high transmission, and flat frequency response (i.e., low dispersion) in a given frequency band can be attained with suitable number of layers. However, broader bandwidth is usually achieved at the expense of increased variation and maximum value of the in-band reflection coefficient, [38].

The layer indexes could be selected in a sequential order, monotonously increasing towards the index of the core medium. In order to facilitate design, one set of the parameters, often optical thickness of the layers, is made fixed, typically to quarter a wavelength in the respective layer at the given operating frequency, [37]. In such a structure, reduction of reflection is achieved, to the first order, by means of destructive interference of the waves reflected from neighboring interfaces. The resulting index distribution along the multilayer stack fits a polynomial regression. As an alternative to the sequential distribution, layer indexes can be chosen arbitrary. This, particularly, in combination with using half-wavelength layers, in the manner of FP interference filters, helps achieve near optimum performance over a broader frequency range under constraint of available index values, [36], [38]-[40].

Multi-layer ARCs have a long heritage of successful applications in optical and quasi-optical devices for millimeter-astronomy, with various fabrication technologies developed. Sputtering of thin polymer films with low energy beams or RF magnetron sputtering of carbon or ceramic films on silicon seem to be impractical at millimeter-wave frequencies, due to required layer thickness, therefore, other techniques are preferred. For low-index polymer components, heat-bonding process to attach dielectric layers to the core was previously investigated, [8]. Heat-bonding also applies for crystalline materials, [41], where ceramic-impregnated dielectric layers can be used. The process works by interleaving the ARC layers and the core with thin low-density polyethylene (LDPE) sheets and hot-pressing the stacked assembly in a thermal cycle tuned for specific selection of materials. The process can be applied for flat and curved surfaces alike. For high-index materials, such as silicon and alumina, epoxy-based coatings, [42] and [43], applied by spin coating on flat surfaces and by epoxy-bonding (e.g., using popular Stycast-series epoxies) of machined or pressed dielectric molds proved to be a viable technology for cryogenic millimeter optics. However, quality of the interfaces and survival of such coatings at cryogenic temperatures still raise concerns.

An innovative technique of plasma sprayed anti-reflection coatings was proposed for cryogenic millimeter-optics elements based on high-index crystalline materials, [44] and [45], particularly, for millimeter astronomy instruments. It has been shown that varying the crystalline powder content and porosity of the sprayed layers fine graded-index coatings could be produced for wide frequency ranges. Such coatings feature improved cryogenic performance, reduced cost, and a high coating rate for large curved surfaces using a robotic arm sprayer. However, this technology was not available for our study. The work outlined in this paper is aimed to develop viable multi-layer ARC solutions for large cold millimeter-optics, including thermal filters and lenses made of low-loss polymer materials.

3.1 Design approach and material constraints

The main constraint for design of broadband multi-layer ARCs for polymer lenses is imposed by available materials. In fact, the range of commercial low-loss polymer films suitable for our design and operation requirements is extremely limited, both in terms of indexes and thicknesses. Materials with proven technology heritage include cast polypropylene (CPP), porous polypropylene (pPP), and porous polytetrafluoroethylene (pPTFE) films. Their thermal and optical performances may vary between suppliers, so that the respective ARC design should allow a room for tolerances. The CPP films has the finest range of thicknesses and could be assembled in stacks closely matching the quarter-wavelength requirement.

For the dielectric indexes and thicknesses available in this work, two optimum ARC structures were designed using the conventional transfer-matrix approach, [36] and [46]. The designs were verified with finite-element analysis simulations using Ansys HFSS High Frequency Simulation Software. The ARC performance was assessed for the case of lossy dielectrics in a representative range of angles of incidence, which also included preliminary sensitivity analysis with respect to the variations in refractive indexes and thicknesses of the layers. The reference values of refractive index and loss-tangent were taken from literature, [9] and [47]. The ARC was applied to both faces of a plane-parallel dielectric slab. The final recipes of the three-layer ARC for the LiteBIRD medium-frequency band of 89 224 GHz the five-layer ARC for the high-frequency band of 166-448 GHz are shown in Table 2.

Table 2. Anti-reflection coating recipes for the LiteBIRD medium-frequency and high-frequency UHMWPE optics devised under the constraint of available dielectric materials.

Layer #	Material	Refractive index	Loss-tangent	3-layer ARC thickness (μm)	5-layer ARC thickness (μm)
	Free space	1	0	Inf.	Inf.
1	Porous PTFE	1.1541	0.0003	450	250
	LDPE	1.5141	0.0003	8	8
2	Cast PP	1.5088	0.0008	110	37
	LDPE	1.5141	0.0003	8	8
3	Porous PTFE	1.1541	0.0003	127	127
	LDPE	1.5141	0.0003	8	8
4	Cast PP	1.5088	0.0008	N/A	67
	LDPE	1.5141	0.0003	N/A	8
5	Porous PTFE	1.1541	0.0003	N/A	55
	LDPE	1.5141	0.0003	N/A	8
	UHMWPE core*	1.5174	0.0003	10020	10020

*- mirror-symmetrical sequence of the ARC layers on the opposite face of the core slab.

3.2 Sample fabrication and measurement

Fabrication of ARC-samples according to the recipes in Table 2 was carried out at Cardiff University with the proprietary polymer heat-bonding process extensively used in manufacturing metal-mesh thermal filters for various astronomical instruments. The samples were hot-pressed under continuous evacuation in a vacuum jig, [8], placed inside a temperature-controlled oven, Fig. 13. The thermal cycle was empirically devised to provide firm layer bonding while preventing sample warping and residual stress in the ARC layers.

Figure 13. A view of the multi-layer ARC sample fabrication using the heat-bonding process.

Two anti-reflection coated samples were fabricated using plane-parallel slugs of the annealed UHMWPE material. The measured thickness of the virgin slugs was 10.02 mm. The final as-pressed thickness of the coated samples was 11.560±0.003 mm (c.f., 11.442 mm nominal thickness of the stack before heat-bonding) with the three-layer ARC, and 11.410±0.010 mm (c.f., 11.172 mm nominal stack thickness) with the five-layer ARC. The discrepancies could have been caused by variation of the thickness of the pPTFE layers.

The fabricated samples were tested for structural integrity by soaking in liquid nitrogen. The quasi-optical transmittance measurements were carried out on both room-temperature and cold samples. Complete set of the results will be published elsewhere, and in this paper only two examples of room-temperature FTS measurements are shown in Fig. 14.

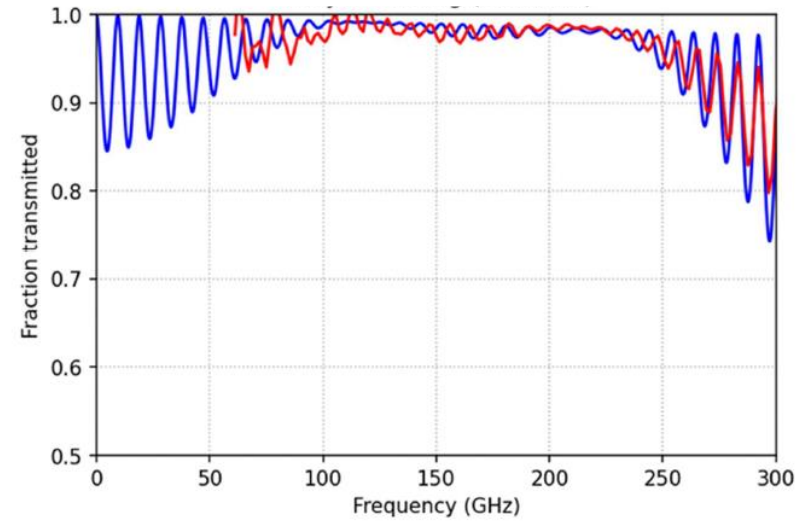

(a)

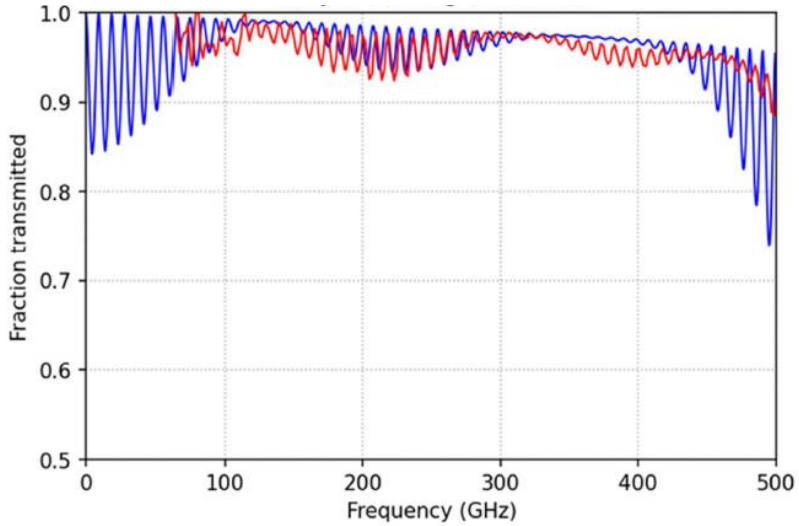

(b)

Figure 14. Room-temperature transmittance of (a) the three-layer and (b) the five-layer anti-reflection coated 10.02 mm UHMWPE slugs. Blue curves represent finite-element simulation with loss, and red curves are FTS measurements.

The measured room-temperature transmittance of the three-layer and five-layer ARC samples demonstrates a reasonably good quantitative agreement with the finite-element analysis simulations. The discrepancies observed, particularly at the

higher frequencies in Fig. 14(b), are attributed to the uncertainties in as-pressed refractive indexes and thicknesses of the coating layers. The work is being carried out on measurements and simulations of cold transmission of the samples, as well as identifying major sources of deviation from the simulated performance. Feasibility of precise characterization of the optical, thermal, and structural properties of individual ARC dielectric layers is being considered. Also, additional test blanks will be fabricated using smaller polymer samples with curved surfaces for thermal cycling tests, before commencing on the manufacture and quasi-optical measurements of large ARC-lenses.

An alternative approach to broadband reduction of reflection from polymer optics involves surface structuring, e.g., [48], and our preliminary simulation results suggest that this can provide a viable solution even in the case of a higher curvature of polymer lenses. This work is in progress, while the next section presents our preliminary results of the development of structured-surface anti-reflection coatings for silicon lenses.

4. STRUCTURED-SURFACE ANTIREFLECTION COATINGS

Structured surface treatment, whereby a surface texture is created by subtracting material to form regular or stochastic surface protrusions, has an obvious advantage over heterogeneous multi-layer coatings, discussed in the previous section, in that there is no mismatch of the thermal properties of the substrate and ARC which would cause structural issues at cryogenic temperatures, [18], [48]-[54]. Besides, silicon at cryogenic temperatures exhibits extremely low loss from millimeter-wave to infrared frequencies, compared to common polymer materials used in multi-layer coatings, hence the structured-surface ARC approach also allows higher optical throughput. Structured-surface ARCs are rapidly becoming more popular solutions for cold millimeter-wave optics of CMB instruments, which is in part due to recent advances in manufacturing. Feasibility of broadband ARC structures on large silicon and alumina optics has been demonstrated using diamond saw dicing, [18], [48], [53], [50], and [54], deep reactive ion etching, [52], and laser ablation, [50] and [51]. Each technique has its own advantages and constraints, c.f., [50], particularly in terms of dimensional and shape precision of the surface features, fabrication defects, and processing time and cost.

The surface features can form a regular two-dimensional array with the period determined by the onset of high-frequency diffraction, viz., [55],

$$\frac{\Lambda}{\lambda} < \frac{1}{max(n_s,n_i)+n_i \sin\theta_{max}}, \tag{3}$$

where Λ is the array period, λ - free-space wavelength, n_s- substrate refractive index, n_i- incident medium refractive index, and θ_{max}- maximum angle of incidence. A square array ensures maximum symmetry and, therefore, minimum cross-polarization and astigmatism, [56] and [57]. It could be noted that in some applications, such as solar photovoltaics, the array period can be chosen so that the ARC is operated in a short-wavelength limit, [58], where the net reflection is suppressed by multiple partial reflections of incident rays at the surfaces of the features, and the incident power is coupled into the substrate by means of total internal reflection or diffraction. Due to the destructive effect on the state of polarization of the propagated beam, this regime is not suitable for CMB optics.

In a long-wavelength, or quasi-static, limit, [58], a two-dimensional array of surface features permits effective homogenization, viz., it can be substituted by a homogeneous, or gradient-index, layer of a fictitious dielectric with an effective refractive index determined by the parameters of the surface features, [18], [55], [56], [58], and [59]. By tapering the shape the surface protrusions along their height, an effective gradient-index medium can be implemented, allowing smooth, nearly reflectionless transition of the incident beam through the structured interface. Theoretically, many shapes of the ARC features are feasible, such as pointed pyramids, flat-top pyramids (frusta), round-tip pyramid etc., with circular, triangular, square, or general polyhedral pyramid bases, [58]. The shape of the pyramid vertical edges, viz., pyramid lateral faces, can also vary from simple linear to general exponential curves. All these variations provide auxiliary degrees of freedom of the design; e.g., using curved-edge pyramids permits a lower height while achieving commensurable reflectivity of taller straight-side pyramids.

The effective medium theory of structured surfaces can also be extended in the second order to the non-quasi-static limit, [60], although it loses its accuracy against a rigorous coupled-wave analysis. Besides, in general, there is no effective refractive index that satisfies with an accuracy both the transmittance and the phase delay in the short-wave limit. Concerning the extraction of the effective index for structured surfaces, it seems the most feasible approach would involve finite-element analysis simulations equating reflection and transmission at the structured-surface interface to that at the interface coated with an equivalent homogeneous or graded-index dielectric layer. It has been noted that the effective

medium theory can yield accurate analytical expressions for the refractive index of one-dimensional arrays of surface features, but even the second-order theory cannot provide adequate analytical expressions for two-dimensional arrays, [55], even in a case of longitudinally uniform protrusions. Still, a number of semi-empirical analytical equations for the effective refractive index of two-dimensional arrays of surface protrusions can be found in literature, e.g., [56] and [58], arguably providing a good starting point for numerical design.

4.1 Design approach and practical constraints

While reserving a proper theoretical analysis and ARC design in the framework of the effective medium theory to our future publications, for the purpose of this paper we adapted the existing solution reported in [50] for a two-dimensional square array of closely packed pyramids with straight edges and flat top. As the substrate material in simulations, HRFZ silicon with the parameters reported in Section 2.3 was used. The array period satisfied the condition (3) precluding the onset of high-frequency diffraction. The pyramid height and top width were numerically tuned for minimum band-averaged reflectance and maximum transmittance using finite-element analysis with Floquet periodic boundary conditions. The optimized LiteBIRD MFT/HFT pyramid dimensions were devised as follows: height $h = 1500/850$ μm; pitch $p = 300/170$ μm; and top width $w = 80/30$ μm. Both designs were verified with finite-element simulations in a representative range of angles of incidence and for various polarization angles with respect to the array axis, showing moderate deterioration of reflectance and negligible cross-polarization. A quick numerical analysis of tolerances on the pyramid dimensions, also introducing a technological gap between the bases of adjacent pyramids, was carried out as well. The systematic presentation of the simulation results will be given in our future paper.

4.2 Sample fabrication

The only technology and expertise for manufacturing the designed ARC structures available at the time and within the budget was dicing-saw cutting, provided by a local vendor. The relatively high aspect ratio of the ARC pyramids required procurement of bespoke beveled dicing blades and preliminary study of blade wear effects. The first working trials of the ARC manufacturing process were carried out on the stock HRFZ-silicon slugs, small enough to fit in the VTT aperture.

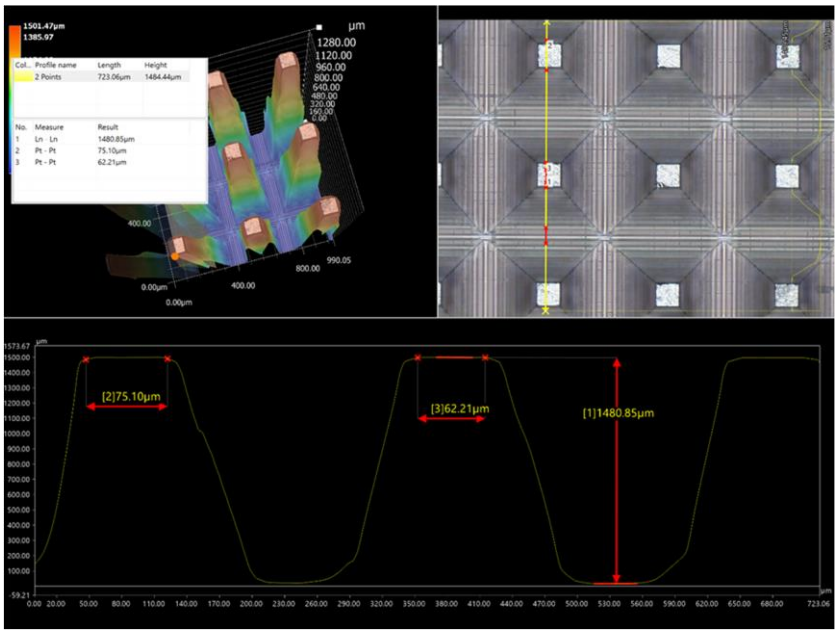

Figure 15. Example screenshots from the optical profilometer illustrating parameters of the ARC pyramids fabricated by dicing-saw cutting according to the MFT recipe (height $h = 1500$ μm; pitch $p = 300$ μm, and top width $w = 80$ μm).

To prepare the ARC-samples for quasi-optical measurements, a stock 12 mm thick HRFZ-silicon slug was mounted in a custom-designed lens holder suitable for cryogenic tests. The slug is held on the side by a flexible aluminum frame glued to the silicon with a Stycast epoxy at several spots. The mounted slug was sent to the ARC machining workshop to apply the MFT coating on both sides.

Initial optical profilometry indicated correct pyramid pitch and nearly correct top width at different locations on the surface. Pyramid tip breakage was minimal. Depth of the cuts and flatness of the valley between adjacent rows of the pyramids were difficult to ascertain initially, due to the highly (optical) reflective surfaces and oblique view. A more comprehensive metrological survey will be carried out using a new optical microscopy system being procured by the research group. Some illustrative images from a commercial optical profilometer are shown in Fig. 15.

4.3 Quasi-optical measurements

The MFT sample of the silicon with ARC cut in both faces was measured on both the VNA (160-260 GHz) and FTS (3-20 cm^{-1}) testbeds. The measured room-temperature transmission is shown in Fig. 16, demonstrating a good quantitative agreement between the two testbeds. The average transmittance is >90% in the MFT band of 89-224 GHz, although the low-frequency FTS irregularities may indicate possible spectrum-recovery issues due to standing waves, or a large-scale quasi-periodic variation of the pyramid parameters due to the blade wear and replacement.

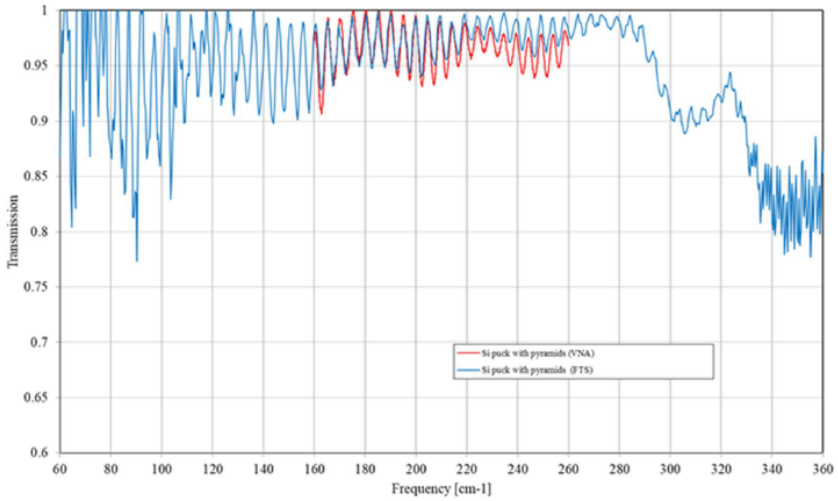

(a)

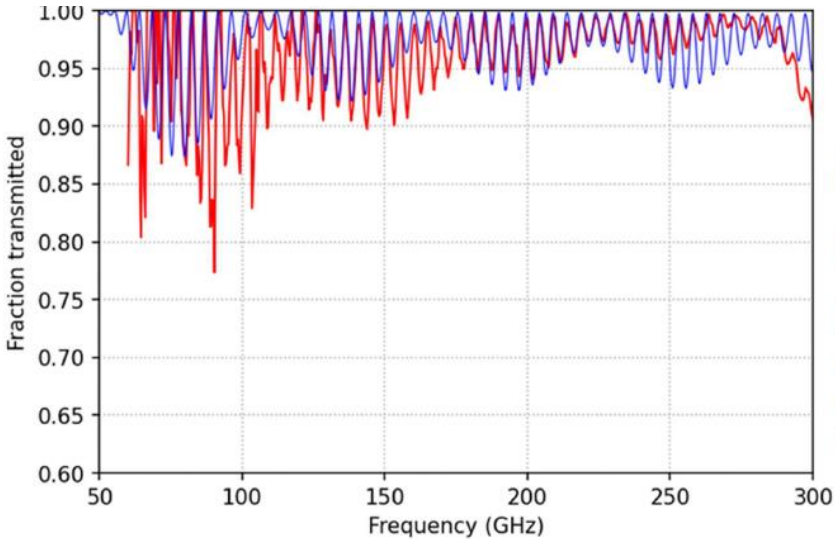

(b)

Figure 16. Room-temperature spectral measurements of the MFT sample of 11.896 mm thick silicon with anti-reflection coating applied to both faces: (a) comparison of the spectral data obtained with the quasi-optical FTS and VNA testbeds; and (b) broadband fringe-fitting of the transmission-line model to the FTS measurements.

The fringe-fitting analysis of the measured data in Fig. 16(b) was carried out using a transmission-line (TL) model code, whereby the square array of ARC pyramids is represented by a cascade of short TL sections forming a tapered impedance transformer, thus emulating a gradient-index effective medium layer, c.f., [18]. The effective characteristic impedance of each TL section is calculated analytically using the first-order effective medium theory applied to the respective regular planar array of square dielectric patches. The transmittance of the effective graded-index layer is fitted to the measurements to retrieve the parameters of the pyramids. Applied to the experimental data in Fig. 16(b), this procedure yields the best-fit values for the pyramid height h = 1450 μm; pitch p = 300 μm, top width w = 50 μm, and valley width x = 50 μm, corresponding to an 86.1° edge slope (c.f., nominal 85.8° edge slope). Hence, our preliminary results show that the envisioned pyramidal ARC on silicon can be fabricated with reasonably high quality at relatively low cost by the commercial dicing-saw cutting process. Next, quasi-optical cold tests on the fabricated MFT sample will be carried out, as well as fabrication, metrology, and spectral testing of the HFT ARC coating recipe on a flat silicon slug. Fabrication and metrology of the ARC coatings on curved silicon surfaces will also be performed.

5. CONCLUSIONS

This paper reports on the up-to-date progress of the development of viable optical solutions for large cryogenic lenses for millimeter-astronomy instruments, particularly, for CMB polarimetry which requires unprecedented knowledge of instrument systematics. The work includes precise broadband characterization of dielectric lens materials, as well as design, manufacturing, and broadband characterization of practical anti-reflection coating solutions for large polymer and crystalline lenses.

New quasi-optical measurements of dielectric parameters have been reported, demonstrating consistency and a good agreement with our previous results and literature data. Two quasi-optical testbeds have been designed, based on either VNA or FTS transmission measurements, with the sample under test placed at a beam waist of the Gaussian beam telescope configuration. New variable temperature testbed was designed and qualified for cryogenic measurements.

Two CMB-telescope lens solutions have been studied: (i) polymer lenses with broadband multi-layer antireflection coatings; (ii) silicon lenses with anti-reflection coating comprising directly machined pyramidal surface structures. It has been shown that both solutions are feasible with commercially available materials and processes. The work is being carried out to identify and test new dielectric materials and surface-texture manufacture technologies which will ultimately provide a broader freedom of design and agility of both solutions to meet ever higher requirements on optical performance of CMB instruments.

Although the manufacturing permits building large-size ARC-lenses, the results presented in this paper are essentially constrained by the capabilities of the quasi-optical testbeds employed, which do not allow measurements of practical lenses. Therefore, a new broadband cryogenic test facility is currently being built, which will comprise a warm compact quasi-optical feed generating a collimated beam transmitted through a large cryostat, capable of accommodating up to 350 mm-diameter optical components, and an automated warm 4-axis field scanning system to map the field in and about the focal plane of a lens under test. The testbed will be operated by a VNA equipped with a range of commercial millimeter-wave frequency extenders. The results of the cryogenic lens measurements will be reported in our future publications.

ACKNOWLEDGEMENTS

This work has been carried out under the European Space Agency Contract No. 4000128517/19/NL/AS. A. Shitvov would like to thank Mr Thomas Gascard of the Astronomy Instrumentation Group, Cardiff University, for reading the manuscript and providing useful comments.

REFERENCES

[1] Allys, E., et al., “Probing cosmic inflation with the LiteBIRD cosmic microwave background polarization survey,” Prog. Theor. Exp. Phys., 2015, 155 pages (2022).
[2] Takahashi, Y. D., et al., “Characterization of the BICEP telescope for high-precision cosmic microwave background polarimetry,” Astrophys. J., 711, 1141-1157 (2010).

[3] Lamagna, L., et al., “The optical design of the LiteBIRD middle and high frequency telescope,” Proc. SPIE 11443-283, 17 pages (2021).
[4] Aikin, R. W., et al., “Optical performance of the BICEP2 telescope at the South Pole,” Proc. SPIE 7741, 77410V-1/10 (2010).
[5] Buchroeder, R. A., “Tilted component optical systems,” PhD Dissertation, University of Arizona (1976).
[6] Rogers, J. D., et al., “Removal of ghost images by using tilted element optical systems with polynomial surfaces for aberration compensation,” Optics Lett., 31(4), 504-506 (2006).
[7] Reshidko, D., and Sasian, J., “Method for the design of nonaxially symmetric optical systems using freeform surfaces,” Opt. Eng., 57(10), 101704 (2018).
[8] Hargrave, P. and Savini, G., “Anti-reflection coating of large-format lenses for sub-mm applications,” Proc. SPIE 7741, 77410S-1/10 (2010).
[9] Hargrave, P., et al., “Critical breadboards manufacture and test report (TN6),” Technical Note PR-6331-08 (ESTEC contract number 4000102522/10/NL/AF), Cardiff University (2013).
[10] Hartwig, G., [Polymer Properties at Room and Cryogenic Temperatures], Springer Science and Business Media LLC (1994).
[11] Baccichet, N., et al., “Detailed characterization of the optical constants of polymers as a function of temperature,” 35th ESA Antenna Workshop, pp. 1-8 (2013).
[12] Hargrave, P. C., et al., “Coated dielectric lens design, modelling and measurements for future CMB polarimetry missions,” 7th Europ. Conf. Anten. Propag. (EuCAP), 1626-1630 (2013).
[13] Dicker, S. R., et al., “Cold optical design for the Large Aperture Simons Observatory telescope,” arXiv:1808.05058 [astro-ph.IM] (2019).
[14] Golec, J. E., et al., “Design and Fabrication of Metamaterial Anti-Reflection Coatings for the Simons Observatory,” arXiv:2101.10298v1 [astro-ph.IM] (2021).
[15] Gudmundsson, J., “Geometrical and physical optics analysis for mm-wavelength refractor telescopes designed to map the cosmic microwave background,” arXiv:1911.13153v1 [astro-ph.IM] (2019).
[16] Chipman, R. A., “Polarization aberrations,” PhD Dissertation, The University of Arizona (1987).
[17] Procter, B., “A study of the effect of thermal history on the internal structure and mechanical properties of polypropylene,” PhD Dissertation, University of Glasgow, UK (1967).
[18] Datta, R., et al., “Large-aperture wide-bandwidth antireflection-coated silicon lenses for millimeter wavelengths,” Appl. Opt., 52(36), 8747-8758 (2013).
[19] Tuominen, E., “Development of Radiation Hard Radiation Detectors – Differences between Czochralski Silicon and Float Zone Silicon,” PhD Dissertation/Internal Report HP-2003-2, Helsinki Institute of Physics, Helsinki, Finland (2003).
[20] Reisz, R. P. and Simon, R., “Reflection of a Gaussian beam from a dielectric slab,” J. Opt. Soc. Am. A, 2(11), 1809-17 (1985).
[21] Pollnau, M. and Eichhorn, M., "Spectral coherence, Part I: Passive resonator linewidth, fundamental laser linewidth, and Schawlow-Townes approximation," Prog. Quant. Electron., 72, 100255 (2020).
[22] Ismail, N., et al., “Fabry-Pérot resonator: spectral line shapes, generic and related Airy distributions, linewidths, finesses, and performance at low or frequency-dependent reflectivity,” Optics Express, 24(15), 16366-89 (2016).
[23] Carnicer, A., et al., “On the longitudinal component of paraxial fields,” Eur. J. Phys., 33(5), 1235 (2012).
[24] Allan, R. N., “Dielectric losses in solids at cryogenic temperatures,” PhD Dissertation, Victoria University of Manchester (1966).
[25] Hara, T., “Dielectric property of some polymers in low temperature region,” Jap. J. Appl. Phys., 6(2), 147-150 (1967).
[26] D'Alessandro, G., et al., ”Ultra High Molecular Weight Polyethylene: optical features at millimeter wavelengths,” Infrared Phys. Technol., preprint, arXiv:1803.05228v1 [astro-ph.IM] (2018).
[27] Lo, Y. H., and Leonhardt, R., “Aspheric lenses for terahertz imaging,” Opt. Express, 16(20), 15991-8 (2008).
[28] Fan, B.W., et al., “Measurement of dielectric constant and loss tangent of several common dielectrics by terahertz time domain spectroscopy,” Proc. of SPIE, 11906, 119060K (2021).
[29] Yamamoto, K., et al., “Degradation diagnosis of ultrahigh-molecular weight polyethylene with terahertz-time-domain spectroscopy,” Appl. Phys. Lett., 85(22), 5194- 5196 (2004).
[30] Chang, T., et al., ”Accurate determination of dielectric permittivity of polymers from 75 GHz to 1.6 THz using both S-parameters and transmission spectroscopy,” Appl. Opt., 56(12), 3287-3292 (2017).

[31] Fedulova, E. V., et al., ”Studying of dielectric properties of polymers in the terahertz frequency range,” Proc. SPIE, 8337, 83370I (2011).
[32] Parshin, V. V., et al. “Silicon as an advanced window material for high power gyrotrons,” Int. J. Infrared Millim. Waves, 16, 863–877 (1995).
[33] Yang, X., et al., “Permittivity of undoped silicon in the millimeter wave range,” Electronics, 8, 886 (2019).
[34] Zhou, K., “Dielectric constant and loss tangent of silicon at 700–900 GHz at cryogenic temperatures,” IEEE Microw. Wireless Comp. Lett. 29 (7), 501-3 (2019).
[35] Mumtaz, M., et al., “Experimental measurement of temperature-dependent sellmeier coefficients and thermo-optic coefficients of polymers in terahertz spectral range,” Optic. Materials, 91, 126-129 (2019).
[36] Orfanidis, S. J., [Electromagnetic Waves and Antennas], Sophocles J. Orfanidis (2016).
[37] Yao, H.-Y., “A design of broadband and low-loss multilayer antireflection coating in THz region,” Prog. Electromag. Research C, 88, 117-131 (2018).
[38] Rabinovitch, K. and Pagis, A., “Multilayer antireflection coatings: theoretical model and design parameters,” Appl. Opt., 14(6), 1326-34 (1975).
[39] Pisano, G., et al., “Experimental realization of an achromatic magnetic mirror based on metamaterials,” Appl. Opt., 55(18), 4814-4819 (2016).
[40] Dobrowolski, J. A., “Optical properties of films and coatings,” in [Handbook of Optics: Volume IV - Optical Properties of Materials, Nonlinear Optics, Quantum Optics], 3rd Edition, Michael Bass (Ed.), The McGraw-Hill Companies, Inc. (2010).
[41] Nadolski, A., et al., “Broadband, millimeter-wave antireflection coatings for large-format, cryogenic aluminum oxide optics,” arXiv:1912.04272v2 [physics.ins-det] (2020)
[42] Rosen, D., et al., “Epoxy-based broadband anti-reflection coating for millimeter-wave optics,” arXiv:1307.7827v1 [astro-ph.IM] (2013).
[43] Lau, J., et al., “Millimeter-wave antireflection coating for cryogenic silicon lenses,” Appl. Opt., 45(16), 3746-51 (2006).
[44] Osbond, P., “Plasma sprayed anti-reflection coatings for microwave optical components,” Adv. Mat., 4(12), 807-9 (1992).
[45] Jeong, O., et al., “Broadband plasma-sprayed anti-reflection coating for millimeter-wave astrophysics experiments,” J. Low Temp. Phys., 184, 621–6 (2016).
[46] P. Yeh, [Optical Waves in Layered Media], Wiley, New York (1988).
[47] Lamb, J., “Miscellaneous data on materials for millimetre and submillimetre optics,” Int. J. Infr. Millim. Waves, 17, 1997-2034 (1996).
[48] Yagoubov, P., et al., “Wideband 67-116 GHz receiver development for ALMA Band 2,” arXiv:1912.10841v3 [astro-ph.IM] (2020)
[49] Wheeler, J. D., et al., “Anti-reflection coatings for submillimeter silicon lenses,” Proc. of SPIE Vol. 9153, 91532Z (2014).
[50] Young, K., et al., “Broadband millimeter-wave anti-reflection coatings on silicon using pyramidal sub-wavelength structures,” arXiv:1702.01768v2 [astro-ph.IM] (2017).
[51] Takaku, R., et al., “Large diameter millimeter-wave low-pass filter made of alumina with laser ablated anti-reflection coating,” Opt. Expr., 29(25), 41745-65 (2021).
[52] Hasebe, T., et al., “Fabrication of three-layer silicon antireflection structures in 200–450 GHz using deep reactive ion etching,”Appl. Phys., 60(33), 10462-67 (2019).
[53] Coughlin, K. P., et al., “Pushing the limits of broadband and high-frequency metamaterial silicon antireflection coatings,” J. Low Temp. Phys., 193, 876–885 (2018).
[54] Nitta, T., et al., “Design, fabrication and measurement of pyramid-type antireflective structures on columnar crystal silicon lens for Millimeter-Wave Astronomy,” J. Low Temp. Phys., 193, 976–983 (2018).
[55] Raguin, D. H. and Morris, G. M., “Antireflection structured surfaces for the infrared spectral region,” Appl. Opt., 32(7), 1154-67 (1993).
[56] Bräuer, R. and Bryngdahl, O., “Design of antireflection gratings with approximate and rigorous methods,” Appl. Opt., 33(34), 7875-82 (1994).
[57] Lamb, J., “Cross-polarization and astigmatism in matching grooves,” Int. J. Infrared Millim. Waves, 17, 2159-65 (1996).
[58] Deinega, A., et al., “Minimizing light reflection from dielectric textured surfaces,” J. Opt. Soc. Am. A, 28(5), 770-777 (2011).

[59] Lalanne, P. and Lemercier-Lalanne, D., “Depth dependence of the effective properties of subwavelength gratings,” J. Opt. Soc. Am. A, 14(2), 450-458 (1997).
[60] Kikuta, H., et al., “Effective medium theory of two-dimensional subwavelength grating in the non-quasi-static limit,” J. Opt. Soc. Am. A, 15(6), 1577-85 (1998).